RSC Advances

PAPER

View Article Online
View Journal | View Issue

Cite this: *RSC Adv.*, 2020, **10**, 17724

Dual-site mixed layer-structured $FA_xCs_{3-x}Sb_2I_6Cl_3$ Pb-free metal halide perovskite solar cells†

Yong Kyu Choi,[a] Jin Hyuck Heo,[a] Ki-Ha Hong *[b] and Sang Hyuk Im *[a]

Received 25th January 2020
Accepted 24th April 2020

DOI: 10.1039/d0ra00787k

rsc.li/rsc-advances

Structure engineering of trivalent metal halide perovskites (MHPs) such as $A_3Sb_2X_9$ (A = a monovalent cation such as methyl ammonium (MA), cesium (Cs), and formamidinium (FA) and X = a halogen such as I, Br, and Cl) is of great interest because a two dimensional (2D) layer structure with direct bandgap has narrower bandgap energy than a zero dimensional (0D) dimer structure with indirect bandgap. Here, we demonstrated 2D layer structured $FACs_2Sb_2I_6Cl_3$ MHP by dual-site (A and X site) mixing. Thanks to the lattice-symmetry change by I–Cl mixed halide, the shortest ionic radius of Cs, and the lower solution energy due to dual-site mixing, the $FACs_2Sb_2I_6Cl_3$ MHP had 2D layer structure and thereby the MHP solar cells exhibited improved short-circuit current density.

Recently, metal halide perovskite solar cells (MHP SCs) have been paid great attention because of their unique properties such as high absorptivity due to direct bandgap, long charge carrier diffusion length, small exciton binding energy, convenient bandgap tunability, and solution processability. Since Kojima *et al.* reported a liquid junction $CH_3NH_3PbX_3$ ($MAPbX_3$, X = I or Br) MHP-sensitized solar cell,[1] intensive studies have been carried out to develop highly efficient MHP SCs.[2–8] Accordingly, the record efficiency of a Pb-based MHP SC reached over 25% under 1 sun conditions (AM1.5G 100 mW cm^{-2}).[9] Although the MHP SCs have great potential in applications such as flexible solar cells, building integrated photovoltaics, vehicle integrated photovoltaics, and portable power generators, the Pb in the MHP SCs causes big problems for finding applications for human-friendly power generators.[10]

Hence, it is big challenging to develop efficient and stable Pb-free MHP SCs. The researches of Pb-free MHP SCs can be roughly classified to divalent metal (Sn and Ge)-based and trivalent metal (Sb and Bi)-based MHP SCs.[11] For instance, Hao *et al.* reported on a 5.7% $MASnBr_xI_{1-x}$ MHP SC composed of F-doped tin oxide (FTO)/blocking TiO_2 (bl-TiO_2)/mesoporous TiO_2 (*m*-TiO_2)/MHP/2,2′,7,7′-tetrakis [*N*,*N*-di(4-methoxyphenyl) amino]-9,9′-spirobifluorene (spiro-OMeTAD)/Au.[12] Recently Jokar *et al.* obtained 9.6% $FASnI_3$ MHP SCs with improved stability by introduction of guanidinium iodide and ethylenediammonium diiodide.[13] Heo *et al.* reported that the phase stability and durability of all inorganic $CsSnI_3$ MHP SCs can be improved by addition of $SnBr_2$.[14] Krishnamoorthy *et al.* reported $AGeI_3$ (A = Cs, MA, and FA ($(NH_2)_2CH$)) MHP SCs.[15] However, the divalent metal (Sn and Ge)-based Pb-free perovskite materials have suffered from their quick oxidation to Sn^{4+}/Ge^{4+} in air atmosphere.[16]

In contrast, the trivalent metal (Bi and Sb)-based MHP SCs with $A_3M_2X_9$ (A = Cs, MA, and FA, M = Sb and Bi, X = Cl, Br, and I) crystal structure exhibit good air and thermal stability.[17–19] However, the $A_3M_2X_9$ MHP SCs have zero dimensional (0D) dimer structure and two dimensional (2D) layer structure. For example, Harikesh *et al.* reported that the formation energies of dimer and layer structure are −12.80 eV and −12.70 eV for $Cs_3Sb_2I_9$ and −12.40 eV and −12.65 eV for $Rb_3Sb_2I_9$ so that the $Cs_3Sb_2I_9$ and $Rb_3Sb_2I_9$ make dimer structure and layer structure, respectively.[20] Similarly, Correa-Baena *et al.* reported that $Cs_3Sb_2I_9$, $Rb_2Sb_2I_9$, and $K_3Sb_2I_9$ have dimer structure with indirect bandgap, layer structure with direct bandgap, and layer structure with indirect bandgap so their power conversion efficiencies (PCEs) are 0.03, 0.76, and 0.07%, respectively.[21] Jiang *et al.* reported that the dimer structured $MA_3Sb_2I_9$ is changed to the layer structured $MA_3Sb_2I_{9-x}Cl_x$ by partial substitution of I to Cl.[22] Umar *et al.* also reported that the dimer structured $MA_3Sb_2I_9$ can be changed to the layer structured $MA_3Sb_2I_{9-x}Cl_x$ by HCl treatment.[23] So far, the bandgaps of $A_3Sb_2X_9$ perovskite materials have been narrowed by structure change from dimer to layer structure owing to the X site mixing of I and Cl. Here, we investigated if the bandgap of layer structured $A_3Sb_2I_6Cl_3$ mixed halide perovskite is controllable by A-site binary mixing of MA, FA, and Cs. Through the systematic studies on the effect of A-site binary mixing on its bandgap, we could find a layer structured $FACs_2Sb_2I_6Cl_3$ perovskite with narrower bandgap than the $MA_3Sb_2I_6Cl_3$ perovskite. In addition, we explained how the dual-site (A-site and X-site) mixed

[a]*Department of Chemical and Biological Engineering, Korea University, 145 Anam-ro, Seongbuk-gu, Seoul 02841, Korea. E-mail: imromy@korea.ac.kr*

[b]*Department of Materials Science and Engineering, Hanbat National University, 125 Dongseo-daero, Yuseong-Gu, Daejeon, 34158, Korea. E-mail: kiha.hong@hanbat.ac.kr*

† Electronic supplementary information (ESI) available. See DOI: 10.1039/d0ra00787k

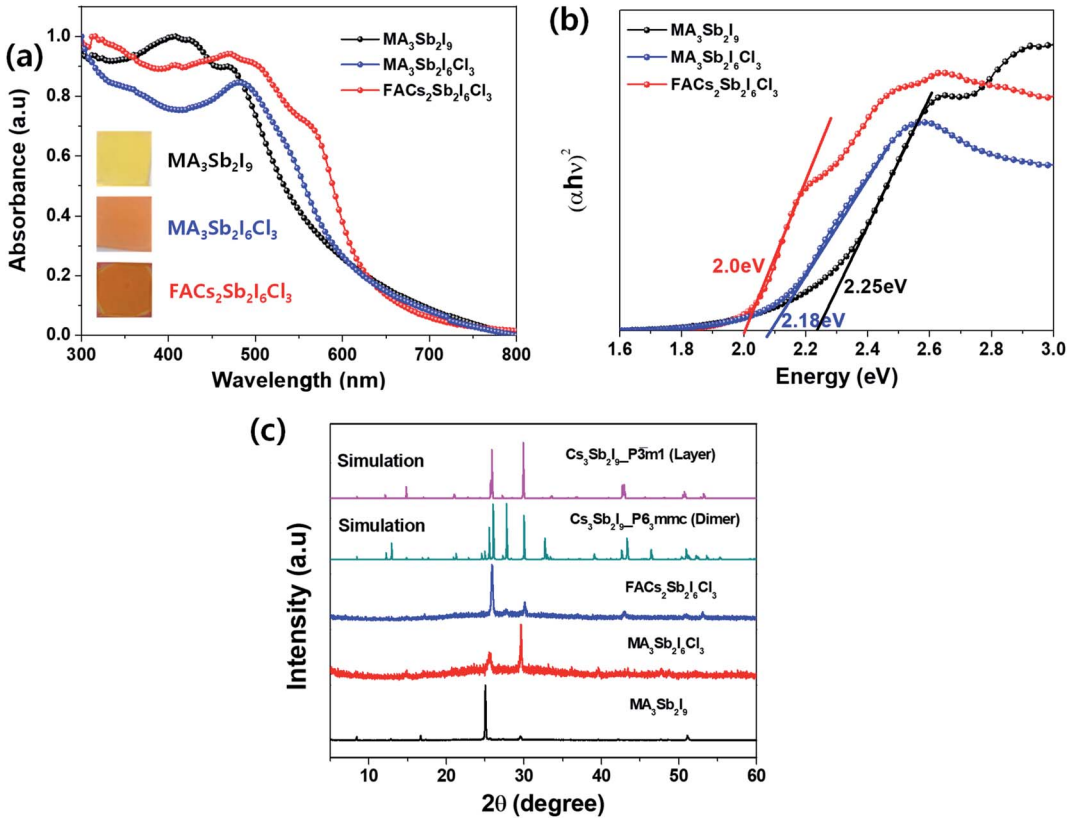

Fig. 1 (a) UV-visible absorption spectra: inset = photographs of the MHP films, (b) Tauc plots, and (c) XRD patterns of $MA_3Sb_2I_9$, $MA_3Sb_2I_6Cl_3$, and $FACs_2Sb_2I_6Cl_3$ MHP films.

$FACs_2Sb_2I_6Cl_3$ perovskite has layer structure and relatively narrow bandgap by density functional theory (DFT) calculation.

To screen what binary combinations of A-site in $A_3Sb_2I_{9-x}Cl_x$ mixed halide perovskite can make narrower bandgap than the $MA_3Sb_2I_6Cl_3$ or $Cs_3Sb_2I_6Cl_3$ perovskite material with ~2.4 eV of bandgap energy, we measured UV-visible absorption spectra and photographs of the $A_3Sb_2I_{9-x}Cl_x$ mixed halide perovskite films as shown in Fig. S1(a)–(d).† Apparently, the $A_3Sb_2I_{9-x}Cl_x$

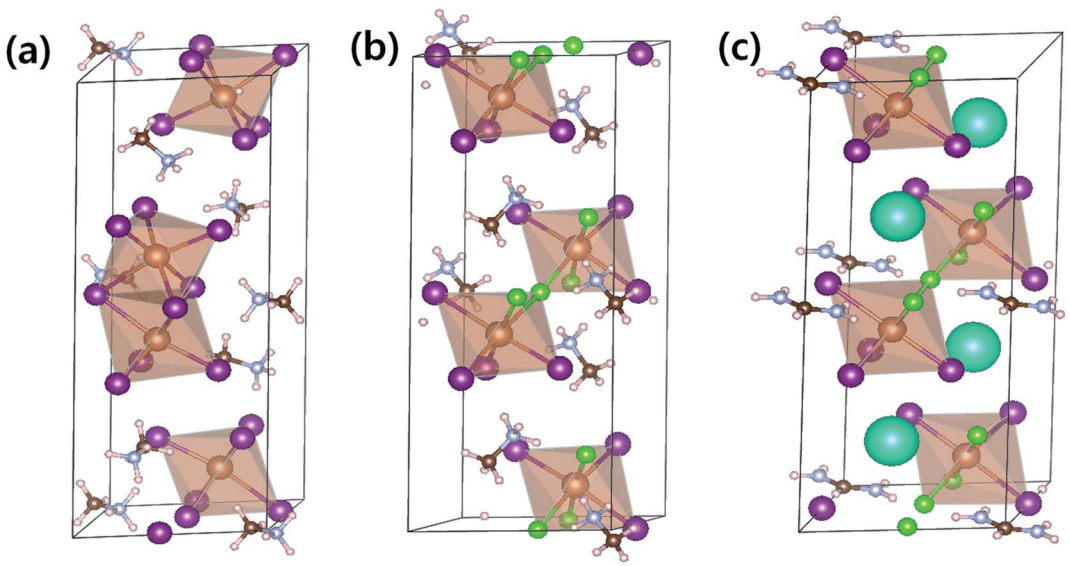

Fig. 2 Lattice structures of (a) $MA_3Sb_2I_9$ ($P6_3/mmc$), (b) $MA_3Sb_2I_6Cl_3$ ($P\bar{3}m1$), and (c) $FACs_2Sb_2I_6Cl_3$ ($P\bar{3}m1$). Pink/brown/light gray/mint/light brown/green/purple spheres represent H/C/N/Cs/Sb/Cl/I respectively.

Table 1 Calculated lattice structures, volume per formula unit (FU), and calculated band gap with spin orbital coupling (SOC) and without SOC

	Calculated lattice structures	Calculated volume/FU Å^3	Calculated band gap (eV)	
			PBEsol	PBEsol + SOC
$MA_3Sb_2I_9$ ($P6_3/mmc$)	$a = 8.637$ Å, $b = 8.475$ Å, $c = 21.246$ Å, $\alpha = 90.8°$, $\beta = 89.4°$ $\gamma = 120.0°$	673.4	1.82	1.69
$MA_3Sb_2I_6Cl_3$ ($P\bar{3}m1$)	$a = 8.077$ Å, $b = 8.362$ Å, $c = 10.233$ Å, $\alpha = 89.9°$, $\beta = 90.8°$ $\gamma = 119.05°$	604.1	1.70	1.55
$FACs_2Sb_2I_6Cl_3$ ($P\bar{3}m1$)	$a = 8.145$ Å, $b = 8.403$ Å, $c = 9.888$ Å, $\alpha = 91.1°$, $\beta = 91.1°$ $\gamma = 118.7°$	593.4	1.67	1.52

mixed halide perovskite films had more red-shifted absorption spectra (Fig. S1(a)–(d)†) than the $A_3Sb_2I_{9-x}Br_x$ perovskites (Fig. S1(e) and (f)†). This implies that the $A_3Sb_2I_{9-x}Cl_x$ mixed halide perovskite films have 2D layer structures and the $A_3Sb_2I_{9-x}Br_x$ perovskites have 0D dimer structures. From the screening experiments, we chose the $FACs_2Sb_2I_6Cl_3$ perovskite material for further studies because it has the most red-shifted absorption spectrum as shown in Fig. S1(c).†

To compare optical properties of the previously reported dimer structured $MA_3Sb_2I_9$ and layer structured $MA_3Sb_2I_6Cl_3$ and the A-sited mixed $FACs_2Sb_2I_6Cl_3$, we measured UV-visible absorption spectra in Fig. 1(a) and plotted corresponding Tauc plots in Fig. 1(b). The inset photographs in Fig. 1(a) indicate that the $MA_3Sb_2I_9$, $MA_3Sb_2I_6Cl_3$, and $FACs_2Sb_2I_6Cl_3$ films have yellow, orange, and brown in color, respectively. The Tauc plots in Fig. 1(b) indicate that the bandgaps of $MA_3Sb_2I_9$, $MA_3Sb_2I_6Cl_3$, and $FACs_2Sb_2I_6Cl_3$ films are 2.25 eV, 2.18 eV, and 2.0 eV, respectively. To check crystal structures of the MHP films, we measured X-ray diffraction (XRD) patterns of the $MA_3Sb_2I_9$, $MA_3Sb_2I_6Cl_3$, and $FACs_2Sb_2I_6Cl_3$ and plotted the simulated XRD reference peaks of $Cs_3Sb_2I_9$ $P6_3/mmc$ 0D dimer structure, of which the $Sb_2I_9^{3-}$ dimers share their triangular faces and form isolated structure,[17,24] and $Cs_3Sb_2I_9$ $P\bar{3}m1$ 2D layer structure, of which the A-site cations act as spacers between the corner-sharing $Sb_2I_9^{3-}$ octahedra,[17,24] as shown in Fig. 1(c) and 2. Similarly to the UV-visible absorption spectra, the $MA_3Sb_2I_6Cl_3$ and $FACs_2Sb_2I_6Cl_3$ exhibited layer structures, whereas the $MA_3Sb_2I_9$ had dimer structure. There were no additional peaks of impurities such as FACl, CsCl, and SbI_3 in the XRD patterns. This indicates that the layer structured MHP films are formed by dual-site mixing.

To understand the thermodynamic origins of dual-site mixing induced phase stabilization for the layered structures, we adopted density functional theory (DFT) using the Vienna *ab initio* simulation package (VASP).[25,26] Details of DFT calculations are summarized in the ESI Section.†

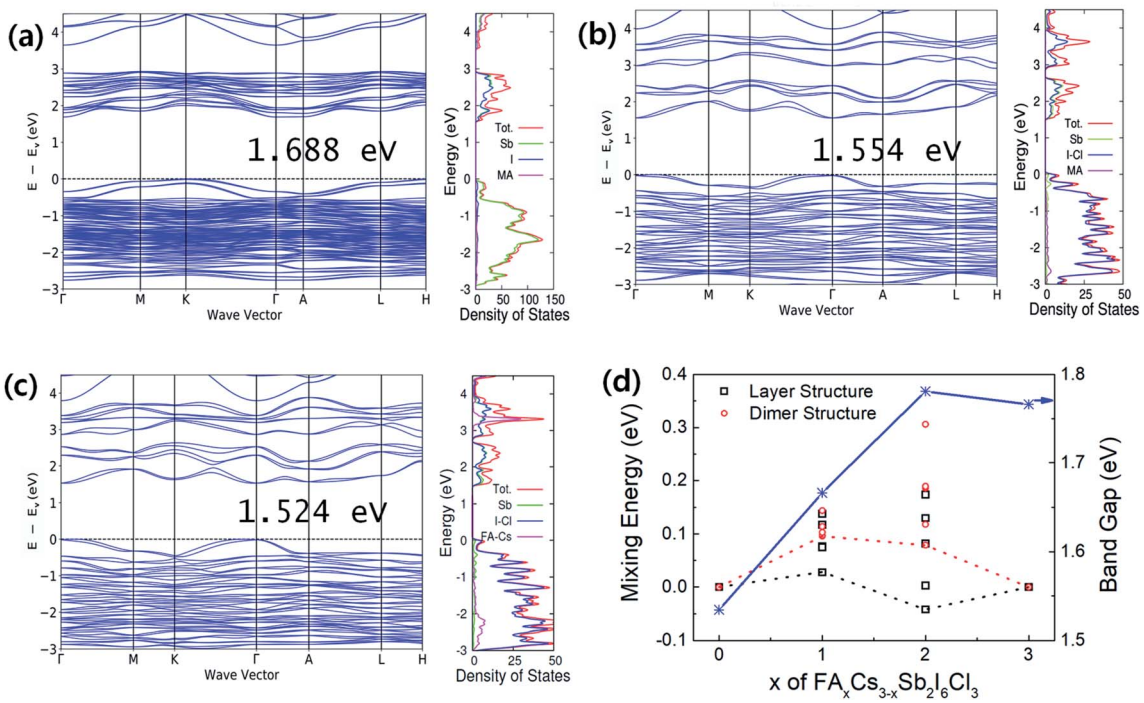

Fig. 3 Band structures (left panel) and projected density of states (PDOS) of (a) $MA_3Sb_2I_9$ ($P6_3/mmc$), (b) $MA_3Sb_2I_6Cl_3$ ($P\bar{3}m1$), and (c) $FACs_2Sb_2I_6Cl_3$ ($P\bar{3}m1$). Valence band maximum energy is set to 0. Spin orbit coupling is included during the calculation. Calculated band gaps are underestimated than those of experimental values. (d) Solution energy changes by A-site mixing of $FA_xCs_{3-x}Sb_2I_6Cl_3$. The dotted lines are connecting the lowest energy states and dispersed symbols represent individual calculation result to obtain optimum lattice structures.

Optimized lattice structures for $MA_3Sb_2I_9$ ($P6_3/mmc$), $MA_3Sb_2I_6Cl_3$ ($P\bar{3}m1$), and $FACs_2Sb_2I_6Cl_3$ ($P\bar{3}m1$) are expressed in Fig. 2 and Table 1.

Band structures and density of states (DOS) are represented in Fig. 3(a–c). The 2D layer structured perovskites ($P\bar{3}m1$) exhibit a more direct band gap like feature comparing with the 0D dimer structured perovskites ($P6_3/mmc$). The calculated band gaps of the perovskites with and without spin orbital coupling (SOC) are summarized in Table 1. The $FACs_2Sb_2I_6Cl_3$ ($P\bar{3}m1$) shows the smallest band gap regardless of SOC considering. The band gap narrowing by I–Cl mixed halide perovskites is attributed to the change of the lattice symmetry, *i.e.*, the phase change from $P6_3/mmc$ to $P\bar{3}m1$.[17,22,27] The reduced band gap for the $FACs_2Sb_2I_6Cl_3$ ($P\bar{3}m1$) can be explained by its shorter bond length than the other perovskites. The volume per formula unit (FU) of $FACs_2Sb_2I_6Cl_3$ ($P\bar{3}m1$) is the smallest even though their lateral dimension is slightly larger than $MA_3Sb_2I_6Cl_3$ ($P\bar{3}m1$) as listed in Table 1. The ionic radius of Cs is the shortest among Cs, MA, and FA so that the volume of $FACs_2Sb_2I_6Cl_3$ can be the smallest. Accordingly, we can think that the $FACs_2Sb_2I_6Cl_3$ has the shortest bond length due to its smallest volume.

The role of A-site binary mixing on the stabilization of 2D layered structure is investigated by calculating solution energies as shown in Fig. 3(d). The solution energies of layered structures are smaller than those of dimer structures. The $FACs_2Sb_2I_6Cl_3$ ($P\bar{3}m1$) has only 28 meV FU^{-1} of solution energy, which can be spontaneous reactions considering the contribution of configurational entropy.[28,29] The DFT calculations clearly show that the dual-site mixing on A and X in $A_3Sb_2X_9$ perovskite can be an efficient way to improve the stability of 2D layer structure and band gap modulation.

To check thermal properties of the dual-site mixed $FACs_2Sb_2I_6Cl_3$ MHP film, we checked thermal gravimetric analysis (TGA) thermogram and differential scanning calorimetry (DSC) as shown in Fig. 4(a) and (b). Here, we prepared the $FACs_2Sb_2I_6Cl_3$ MHP powder by mixing 1 : 2 : 2 molar ratio of FACl : CsCl : SbI_3 instead of mixing 1 : 2 : 1 : 1 molar ratio of FAI : CsI : SbI_3 : $SbCl_3$ because the $SbCl_3$ is more easily sublimed than the SbI_3. The corresponding XRD patterns in Fig. S2† indicate that both samples have layered structures. The TGA and DTA (differential thermal analysis) spectra in Fig. 4(a) and S3† indicate that the FACl and SbI_3 begins to be

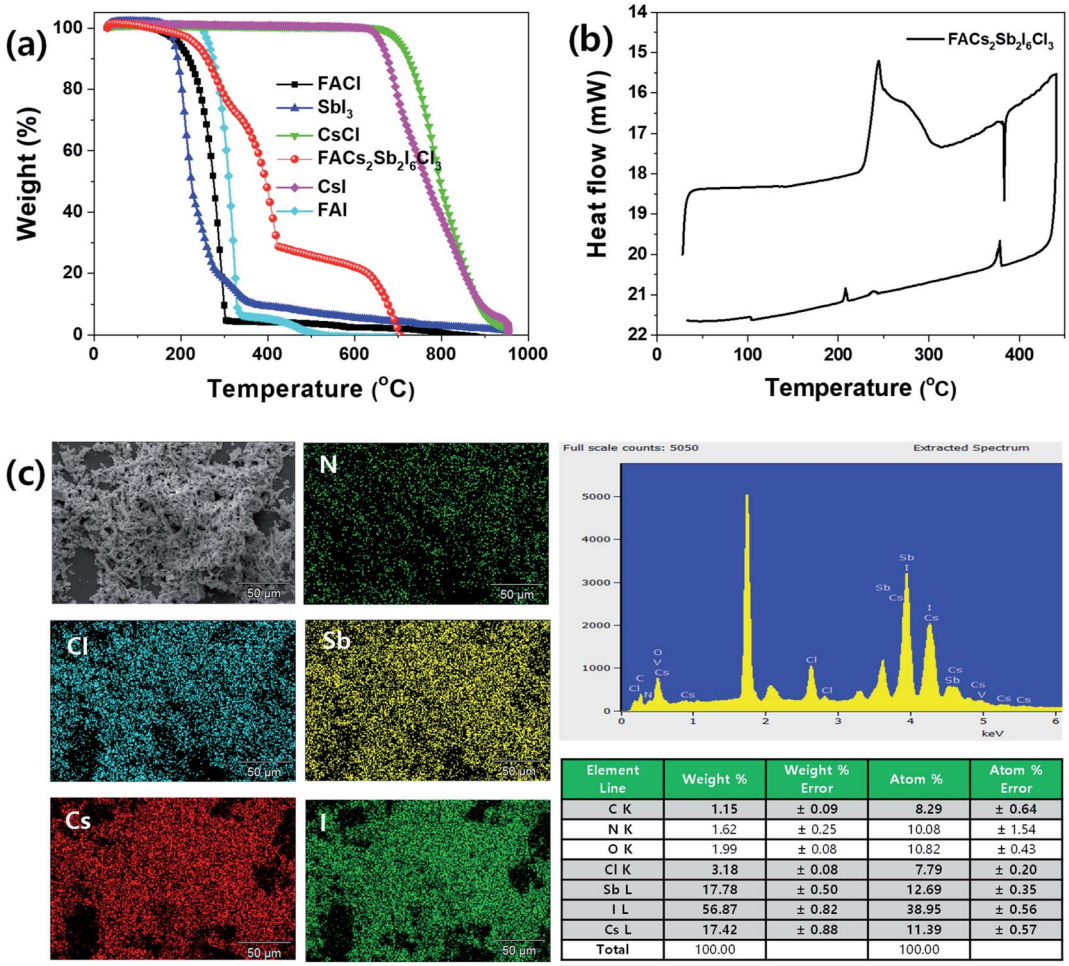

Element Line	Weight %	Weight % Error	Atom %	Atom % Error
C K	1.15	± 0.09	8.29	± 0.64
N K	1.62	± 0.25	10.08	± 1.54
O K	1.99	± 0.08	10.82	± 0.43
Cl K	3.18	± 0.08	7.79	± 0.20
Sb L	17.78	± 0.50	12.69	± 0.35
I L	56.87	± 0.82	38.95	± 0.56
Cs L	17.42	± 0.88	11.39	± 0.57
Total	100.00		100.00	

Fig. 4 (a) Thermogravimetric analysis (TGA) spectra of FACl, SbI_3, CsCl, CsI, FAI and $FACs_2Sb_2I_6Cl_3$ MHP powder, (b) differential scanning calorimeter (DSC) spectra of $FACs_2Sb_2I_6Cl_3$ MHP powder, and (c) energy disperse X-ray spectroscopy (EDS) elemental mapping and spectra of $FACs_2Sb_2I_6Cl_3$ MHP film.

decomposed at ~200 °C, whereas the CsCl starts to be decomposed at ~700 °C. The prepared $FACs_2Sb_2I_6Cl_3$ MHP powder begins to be decomposed at ~230 °C. This implies that the perovskite phase is formed by mixing of 1 : 2 : 2 molar ratio of FACl : CsCl : SbI_3. The weight% of FACl : CsCl : SbI_3 in $FACs_2Sb_2I_6Cl_3$ is 5.67 : 23.67 : 70.66 so the FACl and SbI_3 are decomposed at 230–420 °C and the CsCl is decomposed over 420 °C. The higher decomposition temperature of prepared MHP powder at 150–300 °C than the pure FACl and the lower decomposition temperature of the powder at > 420 °C than the pure CsCl confirms that the new interaction bonding of FA–I and Cs–I is formed by formation of perovskite phase because their decomposition temperatures are FACl < FAI and CsI < CsCI in Fig. 4(a). Some I in the SbI_3 might be replaced with Cl so its composition might be $SbI_{3-x}Cl_x$. Therefore, The $FACs_2Sb_2I_6Cl_3$ MHP powder might show an inflection point at ~310 °C. The DSC spectrum in Fig. 4(b) shows that the synthesized $FACs_2Sb_2I_6Cl_3$ MHP powder begins to be decomposed at ~230 °C, which is consistent with the TGA result.

Fig. 4(c) is energy dispersive X-ray spectroscopy (EDS) elemental mapping and spectrum of the synthesized $FACs_2Sb_2I_6Cl_3$ MHP powder. The Cl, Sb, Cs, and I elements were well dispersed in the EDS elemental mapping image so we can think that the perovskite phase is created. However, the EDS spectrum

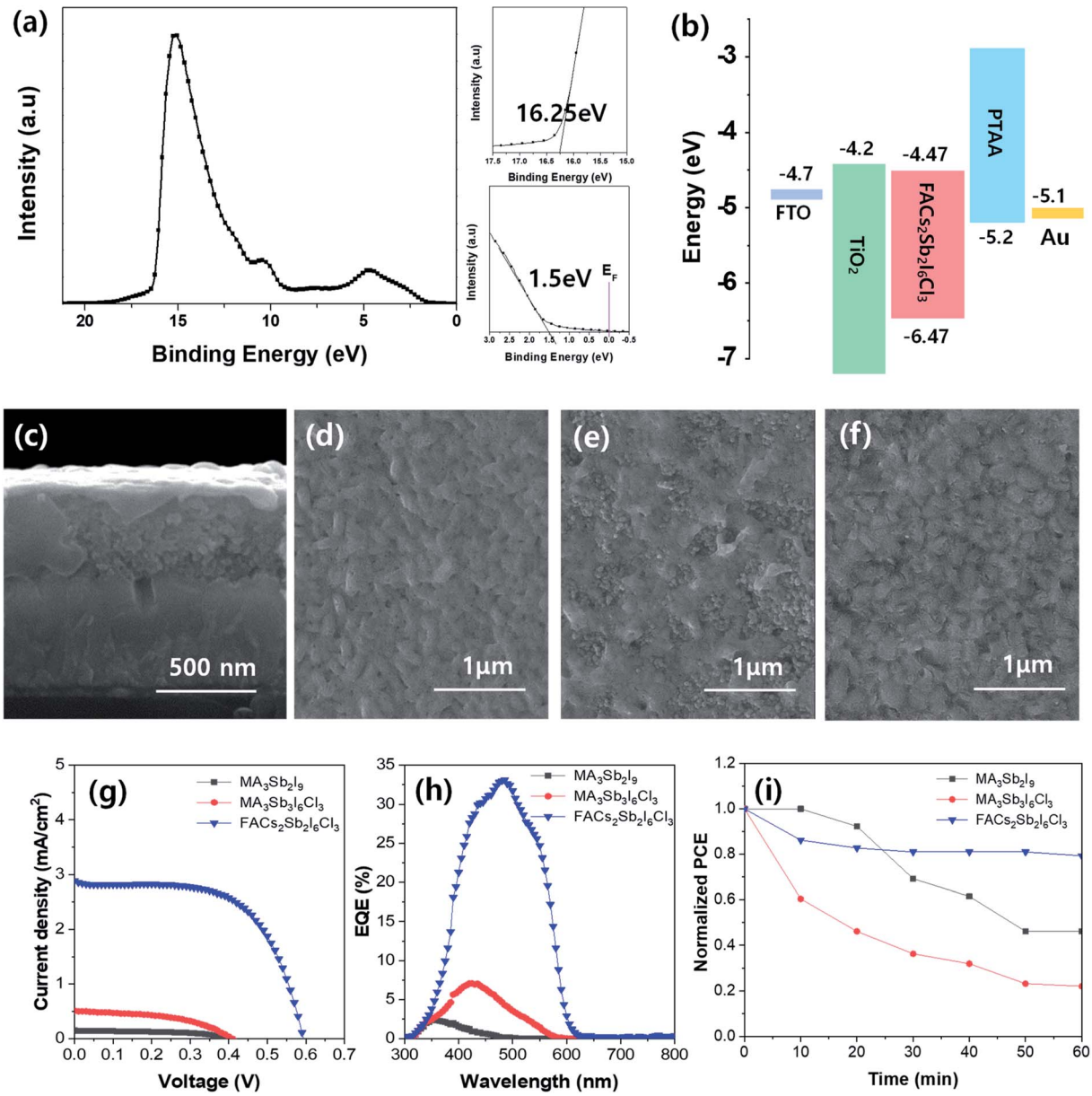

Fig. 5 (a) Ultraviolet photoelectron spectroscopy (UPS) spectrum of $FACs_2Sb_2I_6Cl_3$ MHP film, (b) energy band diagram of MHP SC, (c–f) representative SEM cross-sectional image of MHP SC (c) and SEM surface images (d–f) of FTO/bl-TiO_2/*m*-TiO_2/MHP ((d) $MA_3Sb_2I_9$, (e) $MA_3Sb_2I_6Cl_3$, and (f) $FACs_2Sb_2I_6Cl_3$), and (g–i) photovoltaic properties of MHP SCs: (g) current density–voltage curves, (h) EQE spectra, and (i) stabilities of mesoscopic $MA_3Sb_2I_9$, $MA_3Sb_2I_6Cl_3$, and $FACs_2Sb_2I_6Cl_3$ MHP SCs and planar $FACs_2Sb_2I_6Cl_3$ MHP SC.

indicates that the formed $FACs_2Sb_2I_6Cl_3$ MHP powder is halide deficient because the molar ratio of Cs : Sb : I : Cl was 1.80 : 2.00 : 6.14 : 1.23. This might be attributed to the heat-treatment of the $FACs_2Sb_2I_6Cl_3$ MHP powder at 200 °C for 5 min under nitrogen atmosphere or the oxidation of SbI_3. The UV-visible absorption spectra of the heat treated $FACs_2Sb_2I_6Cl_3$ MHP films at 110 °C, 150 °C, and 200 °C for 5 min under N_2 atmosphere and photographs of corresponding films were shown in Fig. S4(a).† This clearly shows that the film is slightly darken by heat-treatment at 200 °C and its on-set absorption band edge is also slightly red-shifted. Their corresponding XRD patterns in Fig. S4(b)† indicate that their crystalline structures are maintained to 2D layer structure irrespective of heat-treatment temperature. The slightly narrowed XRD peaks by heat-treatment indicate that their crystallinities are slightly improved.

The electronic structure of synthesized $FACs_2Sb_2I_6Cl_3$ MHP film was analyzed by ultraviolet photoelectron spectroscopy (UPS) spectrum as shown in Fig. 5(a). The zoom-up UPS spectra confirm that the onset photoemission and valence band edge is 16.25 eV and 1.50 eV, respectively. Therefore, a calculated valence band maximum (VBM) energy ($E_{VBM} = h\nu - E_{cut\text{-}off} + \Delta E_{VB}$, where $h\nu = 21.22$ eV for He I, $E_{cut\text{-}off} = 16.25$ eV, and $\Delta E_{VB} = 1.50$ eV) of the $FACs_2Sb_2I_6Cl_3$ MHP film is −6.47 eV. The calculated conduction band minimum (CBM) energy is −4.47 eV because its bandgap is 2.0 eV in Tauc plot. The band energy diagram of the TiO_2 electrode based $FACs_2Sb_2I_6Cl_3$ MHP SC was shown in Fig. 5(b). The mesoscopic TiO_2 based MHP SC was composed of FTO/bl-TiO_2/*m*-TiO_2/MHP/PTAA/Au. A representative SEM cross-sectional image of mesoscopic TiO_2 based MHP SC was shown in Fig. 5(c). The SEM surface of $MA_3Sb_2I_9$, $MA_3Sb_2I_6Cl_3$, and $FACs_2Sb_2I_6Cl_3$ film on *m*-TiO_2/bl-TiO_2/FTO substrate were shown in Fig. 5(d–f), respectively. The current density–voltage (*J*–*V*) curves of mesoscopic $MA_3Sb_2I_9$, $MA_3Sb_2I_6Cl_3$, and $FACs_2Sb_2I_6Cl_3$ MHP SCs in Fig. 5(g) indicate that the dual-site mixed $FACs_2Sb_2I_6Cl_3$ MHP SC have the highest PCE than the other MHP SCs. A short-circuit current density (J_{sc}), open-circuit voltage (V_{oc}), fill factor (FF), and PCE of $FACs_2Sb_2I_6Cl_3$ MHP SC was 2.88 mA cm^{-2}, 0.59 V, 61.6%, and 1.05% at 1 sun condition. Their photovoltaic parameters were summarized in Table 2. Average photovoltaic properties of 16 samples for each device were shown in Fig. S5.† The $FACs_2Sb_2I_6Cl_3$ MHP SC did not show significant J-V hysteresis with respect to the scan direction as shown in Fig. S6.† Their external quantum efficiency (EQE) spectra were shown in Fig. 5(h). Although their PCEs are still very poor, it is clear that the dual site-mixed $A_3Sb_2X_9$ MHP SCs have 2D layer structure and narrower bandgap. To check the stabilities of $MA_3Sb_2I_9$, $MA_3Sb_2I_6Cl_3$, and $FACs_2Sb_2I_6Cl_3$ MHP SCs, we tracked the maximum power points (MPPs) of un-encapsulated devices for 60 min under continuous light soaking at 1 sun as shown in Fig. 5(i). This clearly shows that the $FACs_2Sb_2I_6Cl_3$ MHP SC has good stability.

Table 2 Summary of photovoltaic parameters of mesoscopic $MA_3Sb_2I_9$, $MA_3Sb_2I_6Cl_3$, and $FACs_2Sb_2I_6Cl_3$ MHP SCs

Device	J_{sc} (mA cm^{-2})	V_{oc} (V)	FF (%)	PCE (%)
$MA_3Sb_2I_9$	0.162	0.40	55.0	0.03
$MA_3Sb_2I_6Cl_3$	0.51	0.42	47.9	0.10
$FACs_2Sb_2I_6Cl_3$	2.88	0.59	61.6	1.05

Conclusions

In summary, we could synthesize 2D layer structured $FACs_2Sb_2I_6Cl_3$ perovskite with narrower energy bandgap by dual-site mixing. The narrower bandgap of $FACs_2Sb_2I_6Cl_3$ perovskite than the 0D dimer structured $MA_3Sb_2I_9$ and the 2D layer structured $MA_3Sb_2I_6Cl_3$ is attributed to the phase change from $P6_3/mmc$ dimer structure to $P\bar{3}m1$ layer structure due to the change of lattice symmetry by I–Cl mixed halide and the shorter bond length than the others due to the shortest ionic radius of Cs among Cs, MA, and FA. Consequently, the dual-site mixed $FACs_2Sb_2I_6Cl_3$ MHP SCs exhibited higher PCE of 1.05% at 1 sun conditions than the dimer structured $MA_3Sb_2I_9$ MHP SCs and the layer structured $MA_3Sb_2I_6Cl_3$ MHP SCs.

Conflicts of interest

There are no conflicts to declare.

Acknowledgements

This study was supported by the National Research Foundation of Korea (NRF) under the Ministry of Science, ICT & Future Planning (Basic Science Research Program (No. 2014R1A5A1009799), Nano-Material Technology Development Program (No. 2017M3A7B4041696) and the Technology Development Program to Solve Climate Change (No. 2015M1A2A2055631)) and the Ministry of Trade, Industry & Energy, Republic of Korea New & Renewable Energy Core Technology Program of the Korea Institute of Energy Technology Evaluation and Planning (KETEP) (No. 20183010013820).

Notes and references

1 A. Kojima, K. Teshima, Y. Shirai and T. Miyasaka, *J. Am. Chem. Soc.*, 2009, **131**, 6050.
2 M. M. Lee, J. Teuscher, T. Miyasaka, T. N. Murakami and H. J. Snaith, *Science*, 2012, **338**, 643.
3 J. H. Noh, S. H. Im, J. H. Heo, T. N. Mandal and S. I. Seok, *Nano Lett.*, 2013, **13**, 1764.
4 J. H. Heo, S. H. Im, J. H. Noh, T. N. Mandal, C. S. Lim, J. A. Chang, Y. H. Lee, H. J. Kim, A. Sarkar, M. K. Nazeeruddin, M. Grätzel and S. I. Seok, *Nat. Photonics*, 2013, **7**, 486.
5 N. J. Jeon, J. H. Noh, Y. C. Kim, W. S. Yang, S. Ryu and S. I. Seok, *Nat. Mater.*, 2014, **13**, 897.
6 W. S. Yang, J. H. Noh, N. J. Jeon, Y. C. Kim, S. Ryu, J. Seo and S. I. Seok, *Science*, 2015, **348**, 1234.
7 J. H. Heo and S. H. Im, *Nanoscale*, 2016, **8**, 2554.

8 N. J. Jeon, H. Na, E. H. Jung, T. Y. Yang, Y. G. Lee, G. Kim, H. W. Shin, S. I. Seok, J. Lee and J. Seo, *Nat. Energy*, 2018, **3**, 682.
9 NREL, https://www.nrel.gov/pv/assets/pdfs/best-research-cell-efficiencies.20191106.pdf, rev. 11.06.2019.
10 A. Babayigit, A. Ethirajan, M. Muller and B. Conings, *Nat. Mater.*, 2016, **15**, 247.
11 Z. Shi, J. Guo, Y. Chen, Q. Li, Y. Pan, H. Zhang, Y. Xia and W. Hunag, *Adv. Mater.*, 2017, **29**, 1605005.
12 F. Hao, C. C. Stoumpos, D. H. Cao, R. H. Chang and M. G. Kanatzidis, *Nat. Photonics*, 2014, **8**, 489.
13 E. Jokar, C.-H. Chien, C.-M. Tsai, A. Fathi and E. W.-G. Diau, *Adv. Mater.*, 2019, **31**, 1804835.
14 J. H. Heo, J. Kim, H. Kim, S. H. Moon, S. H. Im and K.-H. Hong, *J. Phys. Chem. Lett.*, 2018, **9**, 6024.
15 T. Krishnamoorthy, H. Ding, C. Yan, W. L. Leong, T. Baikie, Z. Zhang, M. Sherburne, S. Li, M. Asta, N. Mathews and S. G. Mhaisalkar, *J. Mater. Chem. A*, 2015, **3**, 23829.
16 W. Liao, D. Zhao, Y. Yu, C. R. Grice, C. Wang, A. J. Cimaroli, P. Schulz, W. Meng, K. Zhu, R.-G. Xiong and Y. Tan, *Adv. Mater.*, 2016, **28**, 9333.
17 B. Saparov, F. Hong, J.-P. Sun, H.-S. Duan, W. Meng, S. Cameron, I. G. Hill, Y. Yan and D. B. Mitzi, *Chem. Mater.*, 2015, **27**, 5622.
18 B.-W. Park, B. Philippe, X. Zhang, H. Rensmo, G. Boschloo and E. M. J. Johansson, *Adv. Mater.*, 2015, **27**, 6806.
19 J. H. Heo, M. H. Lee, D. H. Song, C. E. Song, J.-J. Lee, K.-H. Hong and S. H. Im, *Nanosci. Nanotechnol. Lett.*, 2018, **10**, 591.
20 P. C. Harikesh, H. K. Mulmudi, B. Ghosh, T. W. Goh, Y. T. Teng, K. Thurumal, M. Lockrey, K. Weber, T. M. Koh, S. Li, S. Mhaisalkar and N. Mathews, *Chem. Mater.*, 2016, **28**, 7496.
21 J.-P. Correa-Baena, L. Nienhaus, R. C. Kurchin, S. S. Shin, S. Wieghold, N. T. P. Hartono, M. Layurova, N. D. Klein, J. R. Poindexter, A. Polizzotti, S. Sun, M. G. Bawendi and T. Buonassisi, *Chem. Mater.*, 2018, **30**, 3734.
22 F. Jiang, D. Yang, Y. Jiang, T. Liu, X. Zhao, Y. Ming, B. Luo, F. Qin, J. Fan, H. Han, L. Zhang and Y. Zhou, *J. Am. Chem. Soc.*, 2018, **140**, 1019.
23 F. Umar, J. Zhang, Z. Zin, I. Muhammad, X. Yang, H. Deng, K. Jahangeer, Q. Hu, H. Song, H. Song and J. Tang, *Adv. Opt. Mater.*, 2018, **7**, 1801368.
24 X.-G. Zhao, J.-H. Yang, Y. Fu, D. Yang, Q. Xu, L. Yu, S.-H. Wei and L. Zhang, *J. Am. Chem. Soc.*, 2017, **139**, 2630.
25 G. Kresse and J. Hafner, *Phys. Rev. B: Condens. Matter Mater. Phys.*, 1993, **47**, 558.
26 G. Kresse and J. Furthmüller, *Comput. Mater. Sci.*, 1996, **6**, 15.
27 K.-H. Hong, J. Kim, L. Debbichi, H. Kim and S. H. Im, *J. Phys. Chem. C*, 2017, **121**, 969.
28 F. Brivio, C. Caetano and A. Walsh, *J. Phys. Chem. Lett.*, 2016, **7**, 1083.
29 J. Jeon, T. Eom, E. Lee, S. Kim, S. Kim, K.-H. Hong and H. Kim, *J. Phys. Chem. C*, 2017, **121**, 9508.

